Joule

CellPress

Article

Mechanically Stacked, Two-Terminal Graphene-Based Perovskite/Silicon Tandem Solar Cell with Efficiency over 26%

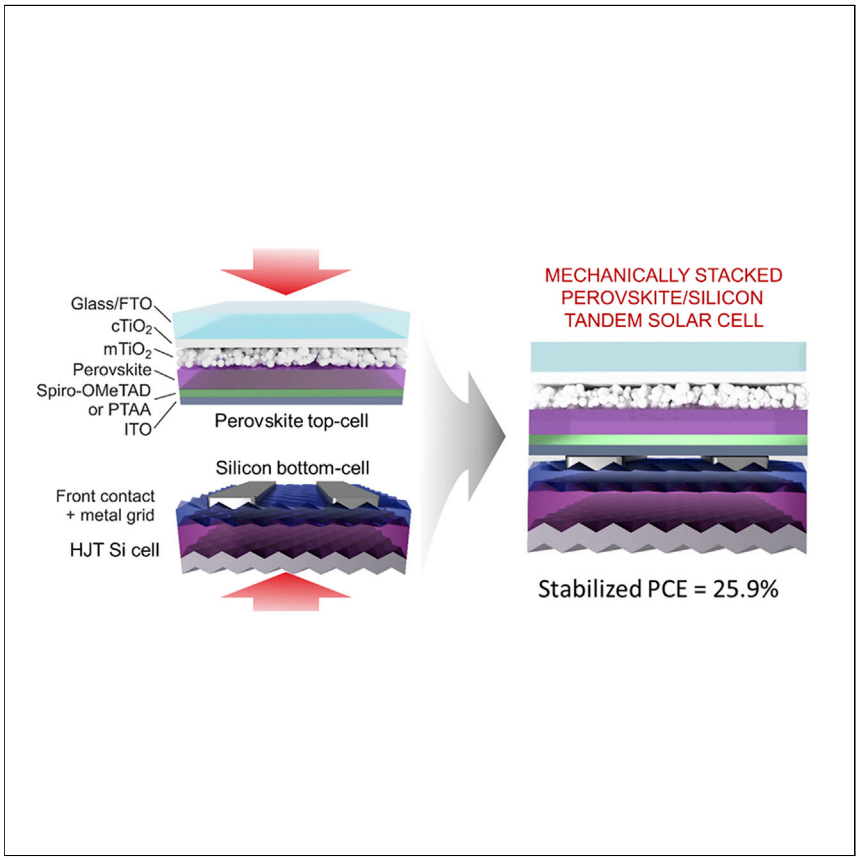

A novel configuration for high-performant perovskite/silicon tandem solar cells is demonstrated using a facile mechanical stacking of the sub-cells. The resulting champion perovskite/silicon tandem solar cell exhibits a stabilized efficiency of 25.9% over an active area of 1.43 cm^2.

Enrico Lamanna, Fabio Matteocci, Emanuele Calabrò, ..., Francesco Bonaccorso, Mario Tucci, Aldo Di Carlo

mario.tucci@enea.it (M.T.)
aldo.dicarlo@uniroma2.it (A.D.C.)

HIGHLIGHTS

Unconventional two-terminal mechanically stacked perovskite/silicon tandem device

Minimized optical losses at the hole selective layer/rear contact of the top cell

Better electrical performance by graphene doping of the electron selective layer

Champion perovskite/silicon tandem with a stabilized PCE of 25.9%

Lamanna et al., Joule 4, 865–881
April 15, 2020
https://doi.org/10.1016/j.joule.2020.01.015

Joule

CellPress

Article

Mechanically Stacked, Two-Terminal Graphene-Based Perovskite/Silicon Tandem Solar Cell with Efficiency over 26%

Enrico Lamanna,[1] Fabio Matteocci,[1] Emanuele Calabrò,[1] Luca Serenelli,[2] Enrico Salza,[2] Luca Martini,[3] Francesca Menchini,[2] Massimo Izzi,[2] Antonio Agresti,[1] Sara Pescetelli,[1] Sebastiano Bellani,[4] Antonio Esaú Del Río Castillo,[4] Francesco Bonaccorso,[4,5] Mario Tucci,[2,*] and Aldo Di Carlo[1,6,7,*]

SUMMARY

Perovskite/silicon tandem solar cells represent an attractive pathway to upgrade the market-leading crystalline silicon technology beyond its theoretical limit. Two-terminal architectures result in reduced plant costs compared to four-terminal ones. However, it is challenging to monolithically process perovskite solar cells directly onto the micrometer-sized texturing on the front surface of record-high efficiency amorphous/crystalline silicon heterojunction cells, which limits both high-temperature and solution processing of the top cells. To tackle these hurdles, we present a mechanically stacked two-terminal perovskite/silicon tandem solar cell, with the sub-cells independently fabricated, optimized, and subsequently coupled by contacting the back electrode of the mesoscopic perovskite top cell with the texturized and metalized front contact of the silicon bottom cell. By minimizing optical losses, as achieved by engineering the hole selective layer/rear contact structure, and using a graphene-doped mesoporous electron selective layer for the perovskite top cell, the champion tandem device demonstrates a 26.3% efficiency (25.9% stabilized) over an active area of 1.43 cm^2.

INTRODUCTION

The current cost of commercially available solar modules is less than 0.5 USD/W_P,[1,2] and the power conversion efficiency (PCE) of the market-leading silicon photovoltaic (PV) technology[3] is gradually approaching its theoretical Auger efficiency limit of 29.4%.[4] The up-to-date record PCE of 26.6%,[5] was obtained by Kaneka Corporation using an interdigitated back contacts (IBC) silicon heterojunction (Si HJT) solar cell.[6] This result is very close to the predicted practical PCE limit of 27%, which also takes into account practical loss mechanisms in large-area silicon devices.[7,8] These loss effects include bulk recombination due to wafer point defects, emitter recombination, edge loss, lateral transport loss, front surface reflectance and absorption, back surface optical loss, and resistive loss.[7,8] Currently, the major cost of the photovoltaic technology is related to the area-dependent balance of system (more than 60% of the average total utility-scale system cost in 2016),[9,10] encompassing wiring, switches, mounting systems, inverters, maximum power point (MPP) tracker, global positioning system (GPS) solar tracker, and, in some cases, solar concentrators and irradiance sensors. It is, therefore, pivotal to increase the PCE in order to lower the Levelized Cost of Electricity of photovoltaics to reach the grid-parity milestone.[10] One approach to upgrading the PCE of silicon technology consists in making silicon-based tandem solar cells, in which a "wide-band-gap solar cell" stacked on

Context & Scale

Perovskite/silicon tandem solar cells promise to push the market-leading crystalline silicon technology beyond its theoretical limit while maintaining low fabrication costs. The possibility to fabricate the perovskite top cell by low-cost solution processing may decrease the levelized cost of energy of photovoltaics toward the grid-parity milestone. However, the solution processing of perovskite solar cells directly onto the textured front surface of high-efficiency amorphous/crystalline silicon heterojunction cells is the main bottleneck. Our simple two-terminal mechanical stacking of the sub-cells helps achieve highly performant PV devices. Its crucial advantage is the possibility to fabricate each sub-cell independently before coupling them. Prospectively, performance improvements and upscaling of perovskite solar cells, as well as the background knowledge on electronic component bonding method, make our results relevant to drive economically feasible perovskite/silicon tandem PVs.

top of the silicon cell can efficiently use high-energy photons to reduce the thermalization losses.[11] In this context, solar cells based on organometal halide perovskite absorbers, namely perovskite solar cells, have been identified as an ideal top-cell candidate for tandem devices with silicon bottom cells.[12–14] *De facto*, perovskite solar cells have witnessed an unprecedented growth among the new generation photovoltaic technologies,[15] with certified PCEs exceeding 23%.[5,16] Moreover, the sharp optical absorption edge and low sub-band-gap absorption of perovskite solar cells,[17] as well as their tunable optical band gap in the ideal range for silicon-based tandem cells (i.e., 1.5–1.8 eV),[18–20] could theoretically allow perovskite/silicon tandem solar cells to achieve PCEs >30%.[12,13,21] Lastly, their solution processability[22,23] enables high-throughput manufacturing and requires a lower capital expenditure (CAPEX), which is important for compensating added marginal costs of tandem solar cells within a short time by increasing their energy production.

In the run-up to disclose commercial products, both two-terminal and mechanically stacked four-terminal perovskite/silicon tandem solar cells have been recently reported to reach PCEs over 25%.[24–28] In principle, monolithic two-terminal devices should provide a higher PCE compared to the four-terminal ones because of the minimization of the number of the electrodes in the stack, each one absorbing ~5%–10% of the incident light.[29] Unfortunately, it is challenging to process the perovskite top cell without altering the optoelectronic quality of the silicon bottom cell or restricting the device design[24,28–32] as well as granting the so-called "current-matching condition" (the same current will flow through both sub-cells with an intensity determined by the least performing one).[33] For example, mesoscopic perovskite solar cells require a high-temperature ($\geq$400°C) processing.[16,34,35] This temperature is not compatible with the state-of-the-art silicon solar cells, namely HJT cells, withstanding temperatures lower than 200°C.[36] Moreover, the textured front side of Si HJT cells,[36] as optimized for infrared light trapping and primary reflection reduction,[24,37] hinders the solution processing of conformal μm-thick perovskite solar cells.[24,28] Experimentally, the front side of Si HJT cells is typically polished, or alternatively not fully solution-based depositions are adopted for the perovskite layer, losing the peculiar feature of both the sub-cells.[24,28–32] Differently from the two-terminal tandem configurations, the four-terminal ones are obtained by mechanically stacking the two sub-cells, which can be fabricated and optimized independently. Moreover, each sub-cell can operate at its respective MPP by using separate tracking systems, making the four-terminal tandem configurations less sensitive to the intensity and spectral change of outdoor illumination compared to the two-terminal ones.[38] To date, the best PCEs that have been achieved with four-terminal tandem configurations are 27.1% from the Interuniversity Micro-Electronics Centre (IMEC) using an IBC Si HJT solar cell[39] and 26.7% by combining perovskite top cells with highly performant passivated emitter with rear locally diffused (PERL) silicon bottom cells.[26] At the time of writing this article, no details have been disclosed by Oxford PV concerning the structure of their monolithic perovskite/silicon tandem devices with a record-high certified PCE of 28%.[40] Despite the manufacturing simplicity and the ease of integration, conventional four-terminal tandem configurations require doubling of all the power electronics and the related installation costs compared to the two-terminal tandem ones.[12] This, inevitably, increases the balance-of-system costs, negatively affecting the levelized cost of energy (LCOE) of the final devices. Therefore, in order to make tandem perovskite/silicon solar cells competitive with silicon single-junction technology, it is crucial to identify a strategy to optimize both of the sub-cells of the two-terminal configurations. The strategy could be the texturing of the silicon bottom cell and the use of high-efficiency perovskite top cells, still using potentially low-cost solution processes for the fabrication of

[1]C.H.O.S.E., Department of Electronic Engineering, University of Rome Tor Vergata, Via del Politecnico 1, 00133 Rome, Italy

[2]ENEA, Casaccia Research Center, Via Anguillarese 301, 00123 Rome, Italy

[3]DIET, University of Rome "Sapienza", Via Eudossiana 18, 00184 Rome, Italy

[4]Graphene Laboratories, Istituto Italiano di Tecnologia, via Morego 30, 16163 Genova, Italy

[5]BeDimensional Spa., Via Albisola 121, 16163 Genova, Italy

[6]Istituto di Struttura della Materia, CNR-ISM, via Fosso del cavaliere 100, 00133 Roma, Italy

[7]Lead Contact

*Correspondence: mario.tucci@enea.it (M.T.), aldo.dicarlo@uniroma2.it (A.D.C.)

https://doi.org/10.1016/j.joule.2020.01.015

the latter. Moreover, it is also important to identify scalable perovskite solar cell technologies that can be practically coupled with commercially available silicon solar cells, typically based on 125 mm (5 inches) or 156 mm (6 inches) square silicon wafers.[41] In this context, graphene and related two-dimensional (2D) materials (GRMs) emerged as a paradigm shift of interface engineering to boost the photovoltaic performance (i.e., PCE and stability) of solution-processed perovskite solar cells and modules.[42–45] Currently, the optoelectronic properties of GRMs can be on-demand tuned by means of morphological modification[46] and chemical functionalization.[47,48] Moreover, GRMs can be produced from the exfoliation of their bulk counterpart in suitable solvents to formulate functional inks,[49] which can be deposited onto different substrates by established printing and/or coating techniques, compatible with solution-based, cost-effective, and large-area manufacturing of perovskite solar cells/modules.[50,51] For example, the incorporation of graphene flakes into the TiO_2-based electron selective layers (typically compact TiO_2 ($cTiO_2$) and mesoporous TiO_2 ($mTiO_2$) dual film) lowers the series resistance, which results in increasing the fill factor (FF) compared to the reference device.[45] Moreover, the addition of graphene to the TiO_2 increases the chemical stability of the perovskite films, which exhibit higher crystalline quality compared to films deposited directly onto pristine $mTiO_2$ and a stable tetragonal phase regardless of the temperature.[52] These effects promote the electron injection at the electron transport layer/perovskite interface, increasing the open circuit voltage (V_{OC}) of the cells,[52] as well as prevent iodine diffusion into the layered cell structure by retarding the $mTiO_2$/perovskite interface degradation,[53] hence extending the lifetime of the devices. According to the theoretical work by Volonakis and Giustino,[54] the graphene/perovskite interface suppress the octahedral tilt in the perovskite crystals leading to a ferroelectric distortion. The interfacial ferroelectricity promotes electron extraction from the perovskite layer and at the same time prevents direct electron-hole recombination across the interface, thus increasing the V_{OC} of the cell.[54]

With the aim to combine the advantages of highly efficient mesoscopic perovskite cells and textured, metalized monocrystalline silicon (c-Si) and Si HJT solar cells into a two-terminal perovskite/silicon tandem device, we report a simple mechanical stacking of the sub-cells fabricated and optimized independently, while preserving the solution processability of the perovskite absorbing layer (Figure 1). A similar concept has been proposed in the literature with a perovskite device laminated onto a silicon cell by a modified PEDOT:PSS interconnecting layer, achieving a two-terminal tandem PCE up to 21%.[55] This approach closely resembles the "wafer bonding" used for the stacking of polished wafers of semiconductors.[56–58] However, it might be a more straightforward method because it does not require extremely clean and polished surfaces to ensure an efficient electrical contact between the sub-parts. In fact, bifacial mesoscopic top cells have been investigated by adopting the fluorine-doped tin oxide (FTO)-coated glasses/$cTiO_2$/$mTiO_2$/perovskite/hole selective layer/indium tin oxide (ITO) structure. Based on our recent works on single-junction (i.e., opaque) mesoscopic perovskite solar cells,[42,43,45,51] we also investigated $cTiO_2$ and $mTiO_2$ doped with graphene flakes to further boost the photovoltaic performance of our bifacial mesoscopic perovskite solar cells.

RESULTS AND DISCUSSION

In agreement with our previously established protocols,[42,43,45,51] $cTiO_2$ and $mTiO_2$ have been prepared by depositing TiO_2 precursor and TiO_2 nanoparticle solutions, respectively, with 1% in volume of graphene flakes dispersion (additional details are reported in Supplemental Information and Experimental Procedures section). Such a

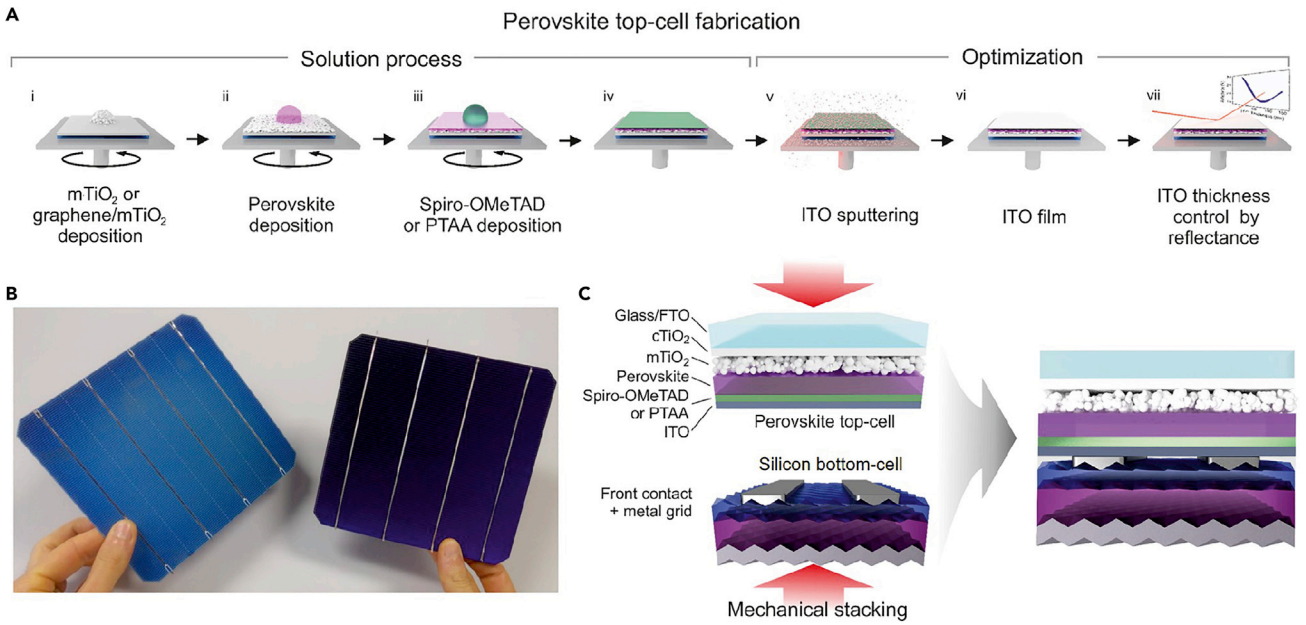

Figure 1. Design and Assembling of the Two-Terminal Perovskite/Silicon Tandem Solar Cells

(A) Solution processing (i–iv) and optoelectronic optimization (v–vii) of a bifacial mesoscopic perovskite top cell.

(B) Commercially available or commercial-like double-side textured and metalized silicon bottom cells (i.e., c-Si and Si-HJT solar cells).

(C) Obtaining the two-terminal perovskite/silicon tandem solar cell by mechanical stacking of sub-cells by applying pressure over their contact area.

small amount of graphene flake doping has been demonstrated to be sufficient for boosting the photovoltaic performance of the mesoscopic perovskite solar cells without altering the optical absorption of the whole device.[42,43,45,51] Among the perovskites, we have opted for a mixed cation, mixed-halide perovskite, i.e., $(Cs_{0.06}FA_{0.78}MA_{0.16})Pb(Br_{0.17}I_{0.83})_3$ because of its optimal optical band gap and improved stability compared to the conventional $MAPbI_3$ perovskite.[59] In fact, the ideal optical band gap of the top-cell absorber over a crystalline silicon solar cell is in the order of 1.7–1.8 eV[13,60] and, for a commercially viable product, its stability should match the over 25-year warranties of silicon-based devices.[59,61,62] More in detail, the optical band gap of $(Cs_{0.06}FA_{0.78}MA_{0.16})Pb(Br_{0.17}I_{0.83})_3$ is 1.64 eV, as estimated by optical absorption and photoluminescence measurements as well as Tauc plot analysis (Figure S1). Although the increase of the Br to I ratio can enlarge the gap of the perovskite toward the ideal values,[18,63] an excess of Br causes photo-induced halide segregation effects.[63] These lead to the formation of iodine-rich domains acting as recombination center traps, which limit the high V_{OC} expected by Br-enriched mixed-halide perovskite solar cells.[63] The perovskite layer was deposited onto the $mTiO_2$ by using a single-step anti-solvent quenching procedure adapted from the literature.[59] Both 2,2′,7,7′-tetrakis(N,N-di-p-methoxyphenylamine)-9,9′-spirobifluorene (spiro-OMeTAD) and the poly[bis(4-phenyl)(2,4,6-trimethylphenyl) amine] (PTAA) have been considered as hole selective layer materials, as mainly exploited in standard and inverted perovskite solar cells, respectively.[64] As shown in Figure S2, the mesoporous perovskite solar cells using the spiro-OMeTAD or PTAA hole selective layer (thickness of 200 and 40 nm, respectively), and a gold (Au) (80 nm) counter electrode, display comparable PCEs (19.0% and 18.6%, respectively). For the realization of the bifacial perovskite solar cells, an ITO counter electrode has been deposited by magnetron sputtering onto the hole selective layer to be subsequently used as the top-cell rear contact (i.e., contacting layer in the perovskite/silicon tandem solar cell). As previously reported, the high kinetic energy of

sputtered ITO particles can damage the underlying organic hole selective layers,[65,66] forming charge extraction barriers at the hole selective layer/counter electrode interface. Therefore, a buffer layer is typically required to protect the organic hole selective layer from damage during sputtering deposition of ITO or other transparent conductive oxides (TCOs). Either thermally evaporated ultrathin layers of Au[65] or sub-stoichiometric molybdenum oxide (MoO_x) buffer layers,[30–32,66–68] have been reported to protect spiro-OMeTAD during TCO sputtering. More recently, SnO_2 has also been exploited both stand alone or in combination with other materials as the buffer layer. In particular, a SnO_2 buffer layer has been deposited through low-temperature (<150°C) atomic layer deposition (ALD) onto an organic underlying layer of inverted perovskite structures sputtering of TCO (e.g., ITO or indium zinc oxide [IZO]) front electrodes.[24,25,29] The combination of SnO_2 and zinc tin oxide (ZTO) in a bilayer structure, deposited by either low-temperature ALD or pulsed chemical vapor deposition (CVD), has also been exploited as buffer layer to minimize parasitic absorption.[69] However, the introduction of either such buffer layers or other aforementioned strategies inevitably add complexity to the perovskite top-cell fabrication process or cause additional optical losses. Moreover, the simplest solution offered by the MoO_x buffer, as exploited also for large-area (16 cm^2) perovskite top cells, has raised concerns over long-term perovskite solar cell stability since the iodide of the perovskite layer chemically reacts with MoO_x, resulting in an unfavorable interface energy level alignment for hole extraction.[70,71] To overcome these hurdles, we have investigated the possibility of avoiding the use of a buffer layer and to deposit the ITO by low-power radio frequency (RF) sputtering directly onto the hole selective layers (either spiro-OMeTAD or PTAA). The ITO sputtering deposition was performed at a power density lower than 0.40 W cm^{-2} with a working pressure of 1.1×10^{-33} mbar using pure Ar gas (without O_2 partial pressure). Optical simulations with the X-ray Oriented Programs (XOP)[72] have been carried out to optimize the thickness of ITO onto both spiro-OMeTAD and PTAA hole selective layers in order to mitigate the parasitic optical losses in the near-infrared (NIR) range (800–1,200 nm wavelength) caused by the light reflection at the hole selective material/ITO interface. The refractive indices (RI) were taken from the literature for spiro-OMeTAD,[73] PTAA,[74] and triple cation perovskites,[75] while the one of ITO has been experimentally measured by refractometry (even though no relevant deviation was observed from the RI reported in reference databases).[76] The thickness of the spiro-OMeTAD and PTAA has been kept fixed at the experimental values of 200 and 40 nm, respectively, to not jeopardize effective charge extraction. These values agree with those previously optimized for high-efficiency and reproducible perovskite solar cells.[16,77,78] Figure 2A shows the dependence of the simulated total average reflectance (AR) of light passing through the perovskite absorber and reaching the hole selective layer/ITO interface on ITO thickness. For the PTAA, a minimum total AR of 16.4% is shown for an ITO thickness of ~80 nm, while for the spiro-OMeTAD the AR monotonically increases with the ITO thickness. Based on the optical simulation outcomes, mesoscopic perovskite top cells based either on spiro-OMeTAD or PTAA have been completed by depositing an 80-nm-thick ITO counter electrode, resulting in a measured sheet resistance of 60 Ω/□. For the case of the spiro-OMeTAD, such thickness of ITO has been selected instead of "less reflective" inferior ones in order to not negatively affect the sheet resistance value. Figure 2B shows the optical transmittances of the optimized spiro-OMeTAD-based and PTAA-based bifacial mesoscopic perovskite subcells. In agreement with the AR simulations, the use of PTAA as the hole selective layer significantly increases the transmittance of the mesoscopic perovskite subcell in the red and NIR light wavelength range compared to that obtained by using the spiro-OMeTAD (by an average of 10.7% between 800–1,200 nm). Furthermore,

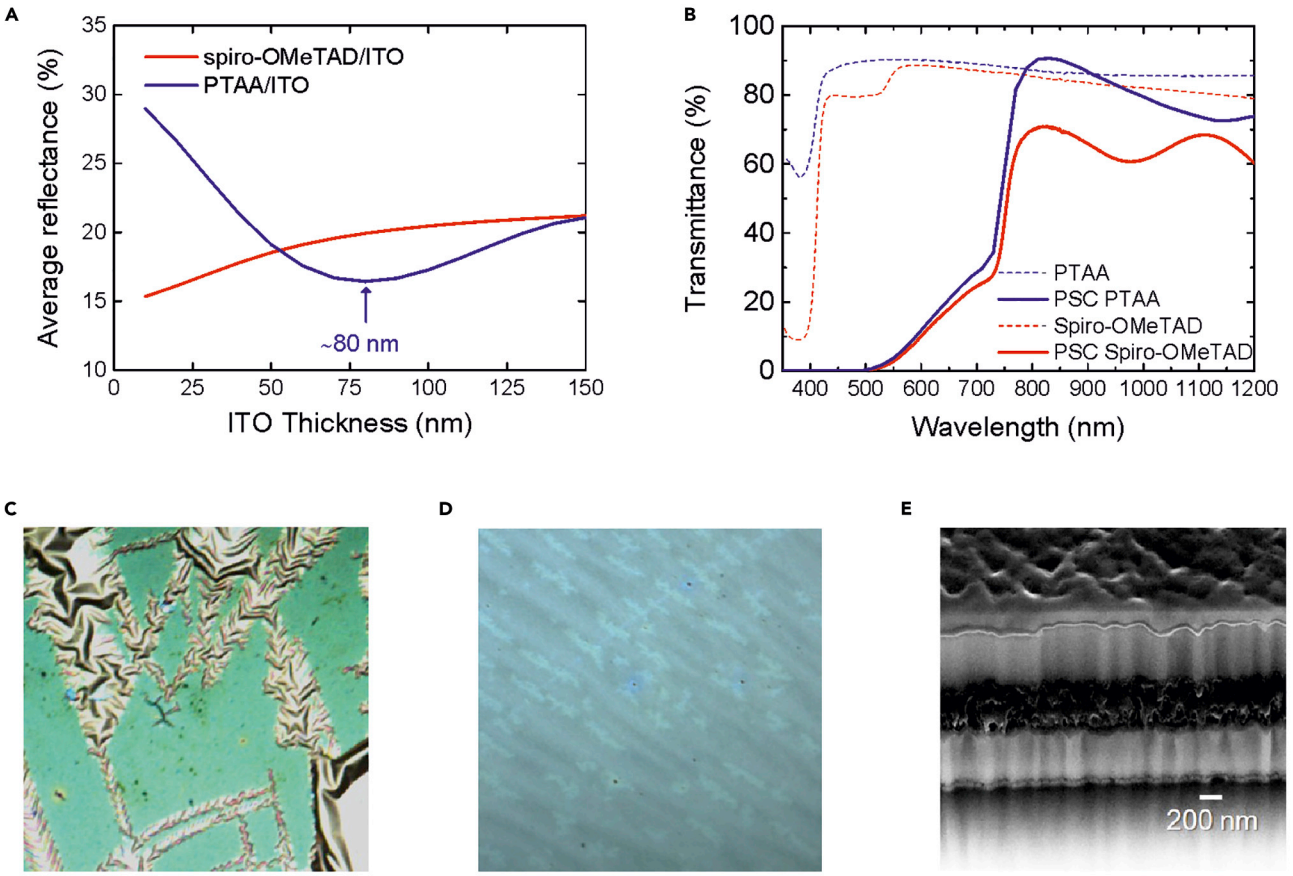

Figure 2. Optics' Optimization and Characterization of the Bifacial Mesoscopic Perovskite Solar Cells

(A) Simulations outcome showing the dependence of the average reflectance (AR) of near-infrared light passing through the perovskite absorber and reaching the hole selective layer/ITO interface on ITO thickness in the bifacial perovskite solar cells.

(B) Optical transmittances of the optimized spiro-OMeTAD-based and PTAA-based bifacial mesoscopic perovskite sub-cells with 80-nm-thick ITO counter electrode. The optical transmittances of spiro-OMeTAD and PTAA layers directly deposited over glass are also shown.

(C and D) Confocal microscope images of 80-nm-thick ITO deposited onto spiro-OMeTAD and PTAA, respectively, showing ITO delamination for the case of spiro-OMeTAD.

(E) Cross-sectional scanning electron microscopy (SEM) of a representative optimized PTAA-based bifacial mesoscopic perovskite top cell with an 80-nm-thick ITO counter electrode.

although the spiro-OMeTAD has been largely exploited as the hole selective layer in bifacial perovskite solar cells,[39,79,80] its parasitic absorption loss in the visible wavelength, as shown by the optical transmission spectrum of a spiro-OMeTAD film deposited on a glass substrate (Figure 2B), has been identified to be a limiting factor for tandem perovskite solar cells.[66,73] In addition to the above optical issues, confocal microscope imaging (Figure 2C) evidenced a poor adhesion of the ITO film over the spiro-OMeTAD and a partial ITO delamination can be observed after exposure of the film to external agents. Differently, the ITO film optimally adheres over the PTAA layer (Figure 2D). These results, together with the analysis of the optical properties of the hole selective layers, have indicated that the PTAA is an ideal hole selective material for the fabrication of the buffer-layer-free bifacial mesoscopic perovskite top cells. The latter is highly desirable for the subsequent two-terminal perovskite/silicon tandem solar cells' fabrication since the absence of the buffer layer minimizes the optical losses, while the mesoscopic structure can prospectively provide current record-high PCEs.[5,16] Figure 2E is a cross-sectional scanning electron microscopy (SEM) image of a representative optimized PTAA-based

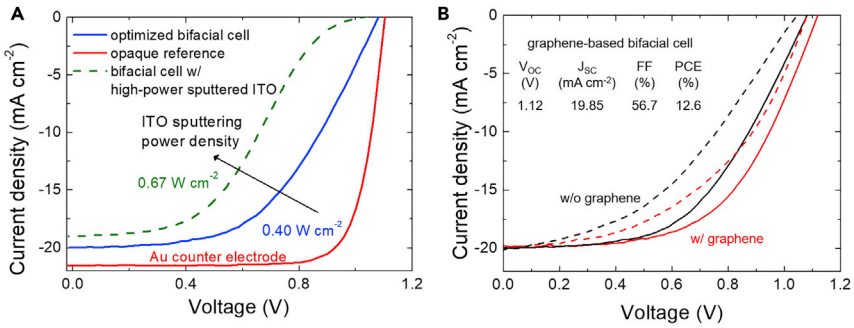

Figure 3. Performance of the Perovskite Top Cells

(A) J-V characteristic measured for the PTAA-based, optimized bifacial mesoscopic perovskite solar cell before addition of graphene flakes into $cTiO_2$ and $mTiO_2$. J-V curves measured for the opaque reference cell using an Au counter electrode and bifacial perovskite solar cells obtained by increasing the power density of the ITO sputtering deposition from 0.40 to 0.67 W cm^{-2} are also shown for comparison.

(B) J-V characteristics measured for the optimized bifacial mesoscopic perovskite solar cells before and after doping the electron selective layer with graphene flakes. The main photovoltaic FoM of the graphene-based bifacial perovskite solar cell are also shown. All the J-V curves have been acquired in reverse voltage scan mode.

mesoscopic perovskite top cell, showing the perovskite solar cell structure. In particular, the 80-nm-thick ITO film is observed over the PTAA layer.

Figure 3A shows the current density-voltage (J-V) characteristic of the optimized PTAA-based semi-transparent mesoscopic perovskite solar cell before adding the graphene flakes into $cTiO_2$ and $mTiO_2$. Such a J-V curve is compared to that measured for an opaque reference cell using an Au counter electrode as well as those measured for the semi-transparent mesoscopic perovskite solar cells obtained by increasing the power density of the ITO sputtering deposition from 0.40 to 0.67 W cm^{-2}. Figure 3B reports the J-V curve measured for the optimized graphene-based mesoscopic perovskite solar cell in comparison to the reference bifacial perovskite device. Table 1 reports the photovoltaic figures of merit (FoM) extracted by the J-V characteristics of those cells.

Before doping the electron selective layer with graphene flakes, the ITO-optimized bifacial mesoscopic perovskite solar cells undergo a 7.3% decrease of the short-circuit current density (J_{SC}) (19.85 mA cm^{-2}) compared to the one of the opaque Au-based reference (21.55 mA cm^{-2}) due to the lack of a back reflection of the light from the metal counter electrode. The high sheet resistance of the ITO counter electrode (~60 Ω/□) of the bifacial perovskite solar cells also negatively affects the FF (52.6%) compared to that of the opaque Au-based reference (78.2%), reducing the PCE of the reference cell from 18.6% to 11.3%. However, we notice here that the sheet resistance of the ITO counter electrode originates high resistive losses on the single-junction perovskite solar cells compared to the two-terminal tandem solar cells. In fact, in the latter, the ITO counter electrode acts similarly to a recombination layer and the photogenerated charges flow vertically to the stack along 80-nm-thick ITO. Contrary, in the single-junction device, the collected photogenerated charges flow in parallel to the electrode layer along a centimetric distance to be collected by the side-located probes. In this view, the two-terminal tandem configuration also relaxes the constraint of the highly conductive top-cell counter electrode required by the four-terminal one, leaving room for ideal optical losses minimization. The photovoltaic performance measured for the optimized bifacial

Table 1. Photovoltaic FoM of the PTAA-Based Mesoscopic Perovskite Solar Cells with Au and Thickness-Optimized (80 nm) ITO Counter Electrodes

Device	V_{OC} (V)	J_{SC} (mA cm^{-2})	FF (%)	PCE (%)
FTO/$cTiO_2$/$mTiO_2$/perovskite/PTAA/Au	1.10	21.55	78.2	18.6
FTO/$cTiO_2$/$mTiO_2$/perovskite/PTAA/ITO[a]	1.08	19.96	52.6	11.3
FTO/$cTiO_2$/$mTiO_2$/perovskite/PTAA/ITO[b]	1.02	18.94	41.0	8.0
FTO/graphene:$cTiO_2$/graphene:$mTiO_2$/perovskite/PTAA/ITO[a]	1.12	19.85	56.7	12.6

[a]RF sputtered at power density = 0.40 W cm^2
[b]RF sputtered at power density = 0.67 W cm^2

mesoscopic perovskite solar cell shows that the optoelectronic properties of PTAA are not altered by the low-power sputtering deposition of ITO. Vice versa, by increasing the power from 0.40 to 0.67 W cm^{-2}, the J-V characteristic of the bifacial mesoscopic perovskite solar cell exhibits an "S-shape." This effect evidences damage of the PTAA/ITO interface, resulting in limited performance (PCE of 8.0%). To further assess the absence of sputtering-induced damage of the polymeric layer, a representative semi-transparent cell was characterized after depositing Au on ITO in order to cancel out resistive losses. Figure S3 shows the comparison between the J-V scans of a perovskite cell based on the PTAA/ITO electrode before and after Au deposition on ITO. Clearly, by depositing Au onto ITO, the sheet resistance of the current collector is drastically decreased compared with the bare ITO film. Consequently, the FF of the cell with Au increases from 38% to 67%. In addition, after Au deposition, the J-V curve does not show a "S-shape," which means that the sputtering of ITO does not damage the underlying structure when PTAA is used as the hole transport material. Lastly, by doping both the $cTiO_2$ and the $mTiO_2$ with graphene flakes, the photovoltaic performances of the optimized graphene-based bifacial mesoscopic perovskite solar cell are further boosted to yield a PCE of 12.6% (+11.5% compared to its graphene-free counterpart), with the V_{OC} and the FF increasing to 1.12 V and 56%, respectively, while there is no variation of the J_{SC} (19.85 mA cm^{-2}) (Figure 3C). The statistical analysis of the photovoltaic FoM of the devices (Figure S4) with and without graphene and with the ITO/Au counter electrode further confirm the beneficial effect of the graphene doping on the V_{OC} and FF of the solar cells.

To assemble the two-terminal tandem perovskite/silicon solar cells, the optimized bifacial mesoscopic perovskite top cell has been mechanically stacked over a silicon bottom cell by applying a pressure of around 1 kg cm^{-2} over the contact area between the two sub-cells (the perovskite solar cell substrate is a 2.5 × 2.5 cm^2 glass). Two types of silicon solar cells have been investigated. The first one is a commercial c-Si solar cell with the screen-printed aluminum back surface field (Al-BSF), while the second one is a Si HJT solar cell (see Supplemental Information for more details). Both types of silicon bottom cells have been provided or finished with screen-printed Ag grids. Consequently, the contact between the two sub-cells is between the Ag grid of the silicon sub-cell and the ITO electrode of the mesoscopic perovskite top cell. Figure S5 shows the cell design and measurement setup for all the tandem devices, including pictures of the stacking rack. Different from the typical two-terminal tandem configurations,[24,29–32] our "mechanical stacking approach" does not require a polished front surface of the silicon bottom cell to enable the subsequent solution processing of the perovskite top cells since the sub-cells are independently fabricated. Moreover, this approach allows us to exploit highly efficient mesoscopic perovskite top cells onto Si HJT bottom cells, which would not withstand the high-temperature (≥400°C) processing of the mesoscopic perovskite solar cells.

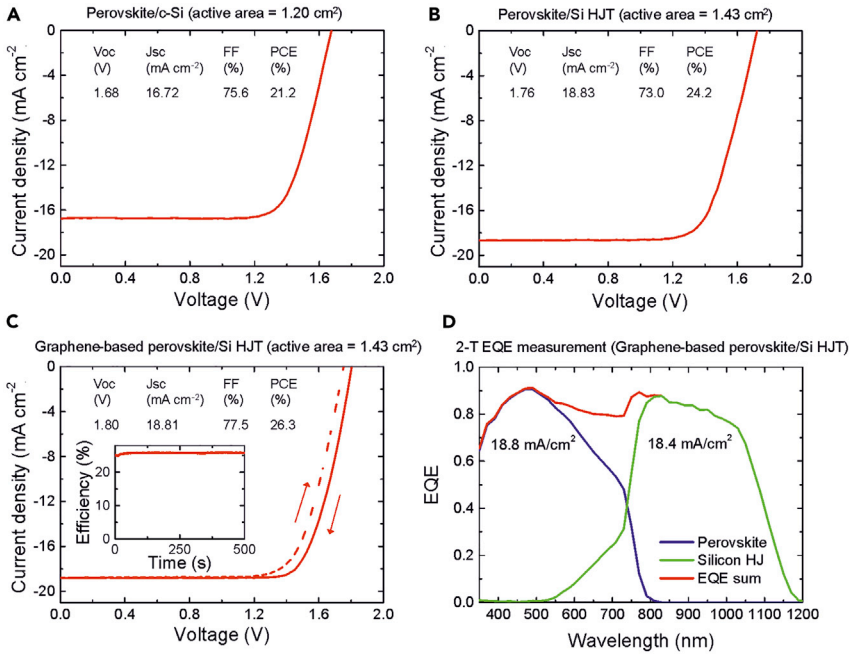

Figure 4. Performance of Mechanically Stacked Two-Terminal Perovskite/Silicon Tandem Solar Cells

(A–C) J-V characteristic of the perovskite/c-Si, perovskite/Si HJT tandem, and graphene-based perovskite/Si HJT tandem solar cells. In (A) and (B), the J-V curves have been measured in reverse voltage scan mode. In (C), both forward and reverse voltage scan mode have been used to measure the J-V curves. The inset to (C) shows the PCE measured over time at the MPP (i.e., the stabilized efficiency).

(D) EQE spectra of the stand-alone graphene-based perovskite and Si HJT sub-cells. The EQE spectrum of the Si HJT cell filtered by the graphene-based perovskite top cell is also shown for the analysis of the "current-matching condition."

The J-V characteristics of the two types of silicon solar cells are reported in Supplemental Information (Figure S6), while those of two-terminal perovskite/silicon tandem solar cells (before graphene addition in mesoscopic perovskite top cells) are shown in Figures 4A and 4B. Figure 4C shows the J-V curve measured for the two-terminal graphene-based perovskite/Si HJT tandem solar cells, which resulted in our most efficient device, as discussed below. Table 2 shows the photovoltaic FoM of the stand-alone silicon bottom cells and the corresponding two-terminal perovskite/silicon tandem solar cells. The perovskite/c-Si tandem solar cell displays a J_{SC} of 16.72 mA cm^{-2}, while the V_{OC} reaches a value of 1.68 V, which approaches the sum of the V_{OC} measured for each sub-cell. The high FF (75.6%) evidences an effective coupling between the two sub-cells: if this were not the case, a higher series resistance would result in the tandem J-V scan, as observed in early attempts using such tandem architecture. Consequently, the PCE of the tandem perovskite/c-Si solar cell (21.2%) shows an increase of 26% compared to that of the stand-alone c-Si bottom cell (16.8%). The two-terminal perovskite/Si HJT tandem solar cell achieves a V_{OC} as high as 1.76 V, which is almost the sum of the V_{OC} measured for each sub-cell. The J_{SC} is also superior to the previous tandem solar cells, thanks to the displacement of the recombination-active contacts from the c-Si provided by the insertion of wide band-gap hydrogenated amorphous silicon between the c-Si and ITO contact.[6,81] Consequently, the perovskite/Si HJT tandem solar cell achieves a PCE of 24.2% (+16% compared to the Si HJT sub-cell). The use of graphene-based mesoscopic perovskite top cells into the most performant two-terminal perovskite/Si HJT tandem configuration further boosts the V_{OC} and the FF up to

Table 2. Photovoltaic FoM of the Stand-Alone Silicon Bottom Cells and the Corresponding Mechanically Stacked Two-Terminal Perovskite/Silicon Tandem Solar Cells

Type of Device	Device	V_{OC} (V)	J_{SC} (mA cm^{-2})	FF (%)	PCE (%)	Area (cm^2)
Stand-alone silicon solar cell	c-Si	0.61	36.80	75.4	16.8	1.20
	Si HJT	0.69	37.57	79.8	20.7	1.43
Two-terminal tandem solar cell	perovskite/c-Si	1.68	16.72	75.6	21.2	1.20
	perovskite/Si HJT	1.76	18.83	73.0	24.2	1.43
	graphene-based perovskite/Si HJT	1.80	18.81	77.5	26.3	1.43

1.80 V and 77.5%, respectively. Consequently, the PCE reaches a value as high as 26.3% (reverse voltage scan). In order to exclude the hysteresis phenomena typically observed in perovskite solar cells[82,83] (e.g., anomalous dependence on the voltage scan direction, rate, or range;[84,85] voltage conditioning history;[86] and device configuration[87]) for the correct estimation of the PCE, J-V curves have also been measured in forward voltage scan mode, resulting in a PCE of 25%. This small hysteresis observed for the tandem cell is actually much less prominent that what is observed for the semi-transparent perovskite devices in Figure 3B. Moreover, the measurement of PCE overtime at the MPP has confirmed a stabilized PCE of 25.9% (inset panel in Figure 4C). Figure S7 reports the forward and reverse J-V scan of a different perovskite/c-Si, without graphene addition, confirming the same marginal hysteresis behavior also for this configuration. The observed behavior is the same in all devices with this tandem architecture. Figure S8 and Table S1 show the statistical analysis of the PCE and the other photovoltaic FoM (estimated by J-V curves in reverse voltage scan mode) measured on 15 graphene-based perovskite/Si HJT tandem solar cells obtained by mechanically stacking different graphene-based mesoscopic perovskite top cells over the same Si HJT bottom cell, showing a mean PCE of 24.9 $\pm$ 0.9%. Additionally, in order to evaluate the long-term stability of our tandem configurations, as well as potential problems caused by the mechanical stacking of the sub-cells, we kept a two-terminal mechanically stacked tandem solar cell under continuously simulated 1 Sun illumination, comparing its photovoltaic performance with that of a reference perovskite solar cell with ITO/Au counter electrode and without encapsulation. Both cells were kept at MPP for the whole duration of the test. As shown in Figure S9, both devices exhibited a similar degradation trend, with the T_{80} (defined as the time the cell reaches 80% of its starting efficiency) being approximately 100 h for both the tandem solar cells and the single perovskite sub-cell. This result exceeds our expectations for the mesoporous structure since the measured T_{80} is comparable to those typically displayed by an encapsulated mesoporous perovskite solar cell in the literature.[88] This suggests that ITO may be an effective barrier to moisture and other degrading agents. Moreover, the similar stability of the here measured samples indicates that the mechanical contact does not represent the current bottleneck in the stability of this tandem configuration, which is still going to be exploitable with more stable p-i-n perovskite top cells.

Figure 4D reports the external quantum efficiency (EQE) spectra for a two-terminal tandem cell comprising a graphene-based mesoscopic perovskite and Si HJT sub-cell, together with the sum of the spectral response of the two sub-cells. The EQE of the Si HJT bottom cell in the IR light wavelength range decreases because of residual parasitic optical losses. The absence of a back reflecting contact on the perovskite top cell also causes a decrease of the EQE at a wavelength longer than 600 nm. Nevertheless, the data show that the "current-matching condition" of the sub-cells is almost perfectly fulfilled, in agreement with the analysis of the FoM extrapolated by the J-V characteristics. The small 0.4 mA cm^{-2} mismatch between

the EQE-integrated current value and the one measured by J-V scan is attributed to the higher impact of the grid shadowing over the rectangular spot area (8 × 5 mm) of the light beam used during the spectral measurement, compared to the case of the fully illuminated cell area during the J-V measurement.

Conclusions

In conclusion, we have reported an innovative and highly efficient two-terminal perovskite/silicon tandem configuration, which is obtained by a simple mechanical stacking of the sub-cells. The two sub-cells are independently optimized to maximize the PCE and, at the same time, to minimize the optical losses within the multiple layers and interfaces. This "mechanical approach" provides a 2-fold advantage. First, any kind of perovskite solar cells, even highly efficient mesoscopic perovskite solar cells, typically processed at high temperature (≥400°C), can be integrated into our two-terminal tandem solar cell design over highly efficient Si HJT bottom cells, which do not withstand temperatures exceeding 200°C. Second, metalized and double-side textured Si HJT bottom cells can be exploited in the two-terminal perovskite/silicon tandem device while preserving the solution processability of the perovskite layer in the perovskite top cell. The latter should be strikingly pursued for cost-effective and high-throughput manufacturing of perovskite solar cells, which is mandatory to compensate added marginal cost of tandem solar cells within a short time by increasing their energy production, i.e., to lower LCOE compared to the current status of photovoltaic technology and the primary energy demand (PED) for the production of devices.[89–91] Bifacial mesoscopic perovskite solar cells have been optimized for their implementation in tandem solar cells by (1) carrying out a low-power sputtering process over a PTAA hole selective layer to preserve its optoelectronic properties during the deposition of the ITO counter electrode without needing a protective oxide-based buffer layer; (2) engineering the optical design by identifying the ideal thickness of the ITO counter electrode to reduce the reflective optical losses at the PTAA/ITO interface; and (3) incorporating graphene flakes into the $cTiO_2$ and $mTiO_2$, used as electron selective layers, in order to lower the series resistance and enhance the electron extraction efficiency. Such optimized bifacial perovskite solar cells have been used as top cells in tandem devices adopting either double-side textured c-Si and Si HJT bottom cells, reaching a champion PCE of 26.3% in reverse voltage scan mode (25.7% in forward voltage scan mode and stabilized PCE of 25.9%) over an active area of 1.43 cm^2. It is noteworthy that higher PCE values are theoretically expected by assuming that PCE of the Si HJT bottom cells are the one achievable on a larger area (>22%). In fact, as demonstrated by record-high PCE of 25.1% measured for both-side-contacted, 151.9 cm^2-area Si HJT solar cells,[92] the PCE on the commercially available large-area Si HJT solar cells is less affected by non-radiative trap-assisted recombination phenomena due to edge defects at the sides of the cell.[81,92] Our "mechanical approach," based on the independent optimization and fabrication of the sub-cells, is ready to synergistically exploit the most recent progress achieved in both perovskite and silicon solar cells, as well as their corresponding modules, in order to propel perovskite/silicon tandem solar cells beyond current photovoltaic technology established in the market.

EXPERIMENTAL PROCEDURES

Solar Cells Fabrication

Perovskite solar cells were fabricated on FTO-coated glass substrates (Pilkington, 8 Ω/□), which were washed by subsequent sonication steps in acetone, ethanol, and isopropanol for 10, 5, and 10 min respectively, in order to remove organic residues from the surface. Silver contacts were screen printed directly over the FTO. These contacts covered and preserved the FTO electrode from the deposition of the subsequent layers. The compact TiO_2 ($cTiO_2$) was deposited by spray pyrolysis

at 450°C starting from a precursor solution of titanium diisopropoxide bis(acetylacetonate), acetylacetone, and ethanol (3:2:45 volume ratio). 10 spray cycles were carried out to achieve a 40-nm-thick layer of $cTiO_2$. The mesoporous TiO_2 ($mTiO_2$) was deposited by spin coating at 3,000 rpm for 15 s a Dyesol 30 NRD titania nanoparticle paste diluted with ethanol in a 1:5 mass ratio. In agreement with previously reported protocols,[43,45] graphene-doped $cTiO_2$ and $mTiO_2$ layers were deposited by the corresponding solution with 1% in volume of graphene flakes dispersion. The latter were produced by liquid-phase exfoliation of graphite flakes in N-methyl-2-pyrrolidone and exchanged into ethanol.[43] The graphene-doped TiO_2 solutions were stirred for 2 h before their deposition. The perovskite precursor solution was prepared by weighting PbI_2, FAI, $PbBr_2$, MABr, and CsI in a vial (1:0.81:0.2:0.16:0.06 material molar ratio), followed by the addition of a dimethylformamide (DMF) and dimethyl sulfoxide (DMSO) solvent mixture in 4:1 respective proportion, in order to obtain a 1.2 M solution of the total material. The deposition was performed in a N_2-filled glove box by spin coating the as-prepared solution with a two-step program at 1,000 and 6,000 rpm for 10 and 20 s, respectively. A chlorobenzene anti-solvent quenching was performed 5 s before the end of the second spin-coating step. Spiro-OMeTAD solution was prepared by dissolving spiro-OMeTAD in chlorobenzene (73.52 mg mL^{-1}) and doping the solution by adding tert-butylpiridine (TBP) (26 μL mL^{-1}) and 16 μL mL^{-1} of a 0.1 M solution of bis(trifluoromethane) sulfonimide lithium salt (Li-TFSI) in acetonitrile. The spiro-OMeTAD solution was deposited onto the perovskite by spin coating at 2,000 rpm for 20 s. Poly(triarylamine) (PTAA) solution was prepared by dissolving 10 mg of the material powder in 1 mL of toluene The PTAA solution was deposited onto the perovskite by spin coating at 3,000 rpm for 20 s. The indium tin oxide (ITO) deposition onto PTAA or spiro-OMeTAD layers was carried out in a linear magnetron radio frequency (RF) sputtering system (Kenosistek), equipped with a load lock chamber. The ITO sputtering process was carried out at a power density of 0.40 or 0.67 W cm^{-2} with a working pressure of 1.1 10^{-3} mbar using pure Ar gas (without O_2 partial pressure). The active area of the perovskite sub-cell was defined by applying a laser-cut 1.2 × 1.2 cm^2 mask for the ITO deposition as shown in Figure S5A. No annealing was performed on the substrates either during the sputtering deposition or after the process.

The Si HJT bottom-cells were fabricated using n-type double-side textured silicon float-zone wafers with a resistivity of 1–5 Ω cm and a thickness of 260 μm. Intrinsic and doped hydrogenated amorphous Si layers were deposited on both sides of the wafer in a RF plasma-enhanced chemical vapor deposition (PECVD) reactor to passivate the Si surface and to create the carrier-selective contacts. N- and p-type doping were achieved by adding PH_3 and B_2H_6 as precursor gasses to SiH_4. Subsequently, ITO was sputtered on both sides by RF magnetron sputtering using Ar gas at a pressure of 10^{-3} bar. Metallization was carried out on both sides by screen-printing deposition of a commercial Ag paste and subsequently cured at 200°C for 10 min. The processed wafers were then cut to 1.2 × 1.2 cm^2 samples.

Commercial c-Si solar cells with Al-SBF were based on p-type monocrystalline Si. The standard front side was passivated by SiN, and the metallization was carried out on both sides by screen-printing deposition of a commercial screen-printable Ag paste and subsequently cured at 200°C for 10 min. For experiments, areas without bus bars and with only metal fingers were cut and used as bottom cells.

For the sub-cell coupling, the glass substrate of the perovskite cell has dimensions 2.5 × 2.5 cm^2 but the active area is only 1.2 × 1.2 cm^2 and determined by the

laser-cut mask used for the sputtering of the ITO; the silicon cell also has the dimensions 1.2 × 1.2 cm^2. The silicon cell is pressed on the active area of the perovskite cell and the whole stack is kept on a rack that holds the cells together. All the setup is shown in Figure S5.

Solar Cell Characterization

The J-V curves of perovskite solar cells were acquired in air atmosphere by using a Keithley 2420 source meter coupled with a solar simulator (ABET Sun 2000, class A), calibrated by a thermopile pyranometer (Pyranometer MS-602, EKO) at AM1.5 and 100 mW cm^{-2} illumination conditions. The voltage step and scan voltage rate were set to 20 mV and 35 mV s^{-1}, respectively. Laser-cut masks of black tape were used to fix the illuminated area at 0.09 cm^2.

The J-V characteristics of both Si solar cells and perovskite/Si tandem solar cells were measured in air atmosphere by using a solar simulator (Class-A WACOM), calibrated at AM1.5 and 100 mW cm^{-2} illumination by a Greatcell Solar Spectrometer. The temperature of the cells was kept at 25°C by means of a cooled holder. The measurements were performed in a four-wire configuration to avoid resistive losses from the measurement circuit.

The electrical measurements of the Si HJT bottom cell were performed directly on the pre-cut 1.2 × 1.2 cm^2 samples (not on the entire wafer). The cut samples included multiple thin metal fingers (not bus bars), as screen printed over the ITO during the cell metallization. The measurement was carried out by applying a probe on each finger of the cell and placing it to the side to avoid the shadowing of the measured active area.

To measure the electrical characteristics of the perovskite/Si tandem solar cells, the ITO back electrode of the perovskite solar cell was simply pressed on the metal grid of the Si solar cell, as schematically shown in Figure 1C of the main text of the manuscript and in Figure S3B. The two cells are aligned by means of a rack. As shown in Figure S5C, the two sides of the rack were screwed together in order to keep the two sub-cells pressed one against the other during the measurement.

EQE spectra were acquired by using a home-made setup composed of a monochromator (Newport, mod. 74000) coupled with a Xe lamp (Oriel Apex, Newport) and a source meter (Keithley, mod. 2612). The light beam spot area is 8 × 5 mm^2. A home-made LabVIEW program was used to control the spectra acquisition. The tandem cell's EQE was measured in the two-terminal configuration by "blinding" the perovskite front cell with a blue light-emitting diode (LED) bias light when measuring the silicon sub-cell and using an IR LED light when measuring the perovskite cell spectral response in order to bias the silicon sub-cell.

Optical absorbance spectroscopy measurements were carried out with a spectrophotometer (PerkinElmer Lambda 950) in the ultraviolet-visible (UV-vis)-NIR spectral range.

Steady-state photoluminescence (PL) measurements were performed with a commercial apparatus (Arkeo – Cicci Research s.r.l.) composed by a charge coupled device spectrometer. The substrates were excited by a green (532 nm) laser at 45° of incidence with a circular spot diameter of 1 mm. A lens condenser attached to a multimode optical fiber bundle composes the optical coupling system.

An X-ray Oriented Program (XOP) was used to optimize the thickness of ITO onto both spiro-OMeTAD and PTAA hole selective layers in order to mitigate the parasitic optical

losses in the near-infrared range (800–1,200 nm wavelength) caused by the light reflection at the hole selective material/ITO interface. More in detail, the perovskite layer was used as reference structure. The investigated structures were subsequently obtained by sequentially stacking the hole selective material (i.e., spiro-OMeTAD or PTAA) and the ITO films. Each layer was optically described in terms of refractive index (n) and extinction coefficient (k) refractive indexes as a function of wavelength and its geometrical thickness. The thickness of the spiro-OMeTAD and PTAA was fixed at the experimental values of 200 and 40 nm, respectively, in agreement with those previously optimized for high-efficiency and reproducible perovskite solar cells (see Results and Discussion in the main text). Lastly, the XOP simulations were performed by using the ITO thickness as variable parameter, resulting in different reflectance profiles. The ITO thickness leading to the lower reflectance profile in the spectral range between 800 and 1,100 nm of wavelength was chosen as the optima one in order to enhance the transmission toward the silicon bottom cells.

SUPPLEMENTAL INFORMATION

Supplemental Information can be found online at https://doi.org/10.1016/j.joule.2020.01.015.

ACKNOWLEDGMENTS

This project has received funding from the European Union's Horizon 2020 Research and Innovation program under grant agreement no. 785219-GrapheneCore2. We gratefully acknowledge the "Accordo di Programma MiSE-ENEA sulla Ricerca di Sistema Elettrico Piano Annuale di Realizzazione 2015" and the University of Rome "Tor Vergata" Mission Sustainability grant "STRAP."

AUTHOR CONTRIBUTIONS

E.L. fabricated and optimized the perovskite top cell. E.L., F.M., E.C., L.S., and L.M. characterized the perovskite solar cells and tandem devices. E.S., L.S., F.M., M.I., and L.M. optimized the ITO sputtering deposition and characterized the resulting films. L.S., M.I., and M.T. fabricated and measured the silicon sub-cells. S.B., A.E.D.R.C., and F.B. produced and characterized the graphene flakes. A.A. and S.P. carried out the engineering of the perovskite device with the addition of graphene and related materials. E.L., F.M., L.S., M.T., and A.D.C. conceived the idea and organized and overviewed the whole activity. E.L., S.B., A.E.D.R.C., F.B., A.A., S.P., and A.D.C. co-wrote the manuscript. S.B. and A.E.D.R.C. elaborated the figures. All the authors have discussed the results and have given approval to the final version of the manuscript.

DECLARATION OF INTERESTS

The authors declare no competing interests.

Received: August 17, 2019
Revised: November 25, 2019
Accepted: January 27, 2020
Published: February 17, 2020

REFERENCES

1. Louwen, A., Van Sark, W., Schropp, R., and Faaij, A. (2016). A cost roadmap for silicon heterojunction solar cells. Sol. Energy Mater. Sol. Cells *147*, 295–314.

2. Verband Deutscher Maschinen- und Anlagenbau, VDMA (2016). International Technology Roadmap for Photovoltaic (ITRPV). VDMA-PV; https://itrpv.vdma.org/en/.

3. Green, M.A., Hishikawa, Y., Warta, W., Dunlop, E.D., Levi, D.H., Hohl-Ebinger, J., and Ho-Baillie, A.W.H. (2017). Solar cell efficiency tables (Version 50). Prog. Photovolt Res. Appl. *25*, 668–676.

4. Richter, A., Hermle, M., and Glunz, S.W. (2013). Reassessment of the limiting efficiency for crystalline silicon solar cells. IEEE J. Photovoltaics *3*, 1184–1191.

5. National Renewable Energy Laboratory (2018). Best research-cell efficiencies. https://www.nrel.gov/pv/cell-efficiency.html.

6. Yoshikawa, K., Kawasaki, H., Yoshida, W., Irie, T., Konishi, K., Nakano, K., Uto, T., Adachi, D., Kanematsu, M., Uzu, H., and Yamamoto, K. (2017). Silicon heterojunction solar cell with interdigitated back contacts for a photoconversion efficiency over 26%. Nat. Energy *2*, 17032.

7. Smith, D.D., Cousins, P., Westerberg, S., Jesus-Tabajonda, R.D., Aniero, G., and Shen, Y. (2014). Toward the practical limits of silicon solar cells. IEEE J. Photovoltaics *4*, 1465–1469.

8. Swanson, R.M. (2005). Approaching the 29% limit efficiency of silicon solar cells. In Conference Record of the IEEE Photovoltaic Specialists Conference, pp. 889–894.

9. Fu, R., Feldman, D., Margolis, R., Woodhouse, M., Ardani, K., Fu, R., Feldman, D., Margolis, R., Woodhouse, M., and Ardani, K. (2017). US Solar photovoltaic system cost benchmark: Q1 2017 (National Renewable Energy Laboratory).

10. Yu, Z.J., Carpenter, J.V., and Holman, Z.C. (2018). Techno-economic viability of silicon-based tandem photovoltaic modules in the United States. Nat. Energy *3*, 747–753.

11. Todorov, T.K., Bishop, D.M., and Lee, Y.S. (2018). Materials perspectives for next-generation low-cost tandem solar cells. Sol. Energy Mater. Sol. Cells *180*, 350–357.

12. Werner, J., Niesen, B., and Ballif, C. (2018). Perovskite/silicon tandem solar cells: marriage of convenience or true love story? – an overview. Adv. Mater. Interfaces *5*.

13. Yu, Z., Leilaeioun, M., and Holman, Z. (2016). Selecting tandem partners for silicon solar cells. Nat. Energy *1*, 16137.

14. Albrecht, S., and Rech, B. (2017). Perovskite solar cells: on top of commercial photovoltaics. Nat. Energy *2*, 16196.

15. Green, M.A., and Ho-Baillie, A. (2017). Perovskite solar cells: the birth of a new era in photovoltaics. ACS Energy Lett. *2*, 822–830.

16. Yang, W.S., Park, B.W., Jung, E.H., Jeon, N.J., Kim, Y.C., Lee, D.U., Shin, S.S., Seo, J., Kim, E.K., Noh, J.H., Seok, S.I.L., et al. (2017). Iodide management in formamidinium-lead-halide-based perovskite layers for efficient solar cells. Science *356*, 1376–1379.

17. De Wolf, S., Holovsky, J., Moon, S.J., Löper, P., Niesen, B., Ledinsky, M., Haug, F.J., Yum, J.H., and Ballif, C. (2014). Organometallic halide perovskites: sharp optical absorption edge and its relation to photovoltaic performance. J. Phys. Chem. Lett. *5*, 1035–1039.

18. Eperon, G.E., Stranks, S.D., Menelaou, C., Johnston, M.B., Herz, L.M., and Snaith, H.J. (2014). Formamidinium lead trihalide: a broadly tunable perovskite for efficient planar heterojunction solar cells. Energy Environ. Sci. *7*, 982–988.

19. Bush, K.A., Frohna, K., Prasanna, R., Beal, R.E., Leijtens, T., Swifter, S.A., and McGehee, M.D. (2018). Compositional engineering for efficient wide band gap perovskites with improved stability to photoinduced phase segregation. ACS Energy Lett. *3*, 428–435.

20. McMeekin, D.P., Sadoughi, G., Rehman, W., Eperon, G.E., Saliba, M., Hörantner, M.T., Haghighirad, A., Sakai, N., Korte, L., Rech, B., et al. (2016). A mixed-cation lead mixed-halide perovskite absorber for tandem solar cells. Science *351*, 151–155.

21. Hörantner, M.T., and Snaith, H.J. (2017). Predicting and optimising the energy yield of perovskite-on-silicon tandem solar cells under real world conditions. Energy Environ. Sci. *10*, 1983–1993.

22. Burschka, J., Pellet, N., Moon, S.J., Humphry-Baker, R., Gao, P., Nazeeruddin, M.K., and Grätzel, M. (2013). Sequential deposition as a route to high-performance perovskite-sensitized solar cells. Nature *499*, 316–319.

23. Nie, W., Tsai, H., Asadpour, R., Blancon, J.C., Neukirch, A.J., Gupta, G., Crochet, J.J., Chhowalla, M., Tretiak, S., Alam, M.A., et al. (2015). High-efficiency solution-processed perovskite solar cells with millimeter-scale grains. Science *347*, 522–525.

24. Sahli, F., Werner, J., Kamino, B.A., Bräuninger, M., Monnard, R., Paviet-Salomon, B., Barraud, L., Ding, L., Diaz Leon, J.J., Sacchetto, D., et al. (2018). Fully textured monolithic perovskite/silicon tandem solar cells with 25.2% power conversion efficiency. Nat. Mater. *17*, 820–826.

25. Chen, B., Yu, Z., Liu, K., Zheng, X., Liu, Y., Shi, J., Spronk, D., Rudd, P.N., Holman, Z., and Huang, J. (2019). Grain engineering for perovskite/silicon monolithic tandem solar cells with efficiency of 25.4%. Joule *3*, 177–190.

26. Ramírez Quiroz, C.O., Shen, Y., Salvador, M., Forberich, K., Schrenker, N., Spyropoulos, G.D., Heumüller, T., Wilkinson, B., Kirchartz, T., Spiecker, E., et al. (2018). Balancing electrical and optical losses for efficient 4-terminal Si-perovskite solar cells with solution processed percolation electrodes. J. Mater. Chem. A *6*, 3583–3592.

27. Lal, N.N., Dkhissi, Y., Li, W., Hou, Q., Cheng, Y.B., and Bach, U. (2017). Perovskite tandem solar cells. Adv. Energy Mater. *7*, 1602761.

28. Jošt, M., Köhnen, E., Morales-Vilches, A.B., Lipovšek, B., Jäger, K., Macco, B., Al-Ashouri, A., Krč, J., Korte, L., Rech, B., et al. (2018). Textured interfaces in monolithic perovskite/silicon tandem solar cells: advanced light management for improved efficiency and energy yield. Energy Environ. Sci. *11*, 3511–3523.

29. Bush, K.A., Manzoor, S., Frohna, K., Yu, Z.J., Raiford, J.A., Palmstrom, A.F., Wang, H.P., Prasanna, R., Bent, S.F., Holman, Z.C., and McGehee, M.D. (2018). Minimizing current and voltage losses to reach 25% efficient monolithic two-terminal perovskite-silicon tandem solar cells. ACS Energy Lett. *3*, 2173–2180.

30. Wu, Y., Yan, D., Peng, J., Duong, T., Wan, Y., Phang, S.P., Shen, H., Wu, N., Barugkin, C., Fu, X., et al. (2017). Monolithic perovskite/silicon-homojunction tandem solar cell with over 22% efficiency. Energy Environ. Sci. *10*, 2472–2479.

31. Peng, J., Duong, T., Zhou, X., Shen, H., Wu, Y., Mulmudi, H.K., Wan, Y., Zhong, D., Li, J., Tsuzuki, T., et al. (2017). Efficient indium-doped TiO x electron transport layers for high-performance perovskite solar cells and perovskite-silicon tandems. Adv. Energy Mater. *7*, 1601768.

32. Albrecht, S., Saliba, M., Correa Baena, J.P., Lang, F., Kegelmann, L., Mews, M., Steier, L., Abate, A., Rappich, J., Korte, L., et al. (2016). Monolithic perovskite/silicon-heterojunction tandem solar cells processed at low temperature. Energy Environ. Sci. *9*, 81–88.

33. Almansouri, I., Ho-Baillie, A., Bremner, S.P., and Green, M.A. (2015). Supercharging silicon solar cell performance by means of multijunction concept. IEEE J. Photovoltaics *5*, 968–976.

34. Cho, K.T., Paek, S., Grancini, G., Roldán-Carmona, C., Gao, P., Lee, Y., and Nazeeruddin, M.K. (2017). Highly efficient perovskite solar cells with a compositionally engineered perovskite/hole transporting material interface. Energy Environ. Sci. *10*, 621–627.

35. Tonui, P., Oseni, S.O., Sharma, G., Yan, Q., and Tessema Mola, G. (2018). Perovskites photovoltaic solar cells: an overview of current status. Renew. Sustain. Energy Rev. *91*, 1025–1044.

36. Battaglia, C., Cuevas, A., and De Wolf, S. (2016). High-efficiency crystalline silicon solar cells: status and perspectives. Energy Environ. Sci. *9*, 1552–1576.

37. Holman, Z.C., Filipič, M., Descoeudres, A., De Wolf, S., Smole, F., Topič, M., and Ballif, C. (2013). Infrared light management in high-efficiency silicon heterojunction and rear-passivated solar cells. J. Appl. Phys. *113*, 13107.

38. Futscher, M.H., and Ehrler, B. (2017). Efficiency limit of perovskite/Si tandem solar cells. ACS Energy Lett. *1*, 863–868.

39. Jaysankar, M., Raul, B.A.L., Bastos, J., Burgess, C., Weijtens, C., Creatore, M., Aernouts, T., Kuang, Y., Gehlhaar, R., Hadipour, A., and Poortmans, J. (2019). Minimizing voltage loss in wide-bandgap perovskites for tandem solar cells. ACS Energy Lett. *4*, 259–264.

40. Oxford PV (2018). Oxford PV perovskite solar cell achieves 28% efficiency. https://www.oxfordpv.com/news/oxford-pv-perovskite-solar-cell-achieves-28-efficiency.

41. Fisher, G., Seacrist, M.R., and Standley, R.W. (2012). Silicon crystal growth and wafer technologies. Proc. IEEE *100*, 1454–1474.

42. Agresti, A., Pescetelli, S., Palma, A.L., Del Rio Castillo, A.E., Konios, D., Kakavelakis, G., Razza, S., Cinà, L., Kymakis, E., Bonaccorso, F., et al. (2017). Graphene interface engineering for perovskite solar modules: 12.6% power conversion efficiency over 50 cm 2 active area. ACS Energy Lett. *2*, 279–287.

43. Agresti, A., Pescetelli, S., Taheri, B., Del Rio Castillo, A.E., Cinà, L., Bonaccorso, F., and Di Carlo, A. (2016). Graphene–perovskite solar cells exceed 18 % efficiency: A stability study. ChemSusChem *9*, 2609–2619.

44. Najafi, L., Taheri, B., Martín-García, B., Bellani, S., Di Girolamo, D., Agresti, A., Oropesa-

Nuñez, R., Pescetelli, S., Vesce, L., Calabrò, E., et al. (2018). MoS2 quantum dot/graphene hybrids for advanced interface engineering of a CH3NH3PbI3 perovskite solar cell with an efficiency of over 20%. ACS Nano *12*, 10736–10754.

45. Agresti, A., Pescetelli, S., Najafi, L., Del Rio Castillo, A.E., Oropesa-Nunez, R., Busby, Y., Bonaccorso, F., and Di Carlo, A. (2017). Graphene and related 2D materials for high efficient and stable perovskite solar cells. In IEEE 17th International Conference on Nanotechnology (IEEE-NANO), pp. 145–150.

46. Terrones, M., Botello-Méndez, A.R., Campos-Delgado, J., López-Urías, F., Vega-Cantú, Y.I., Rodríguez-Macías, F.J., Elías, A.L., Muñoz-Sandoval, E., Cano-Márquez, A.G., and Charlier, J.C. (2010). Graphene and graphite nanoribbons: morphology, properties, synthesis, defects and applications. Nano Today *5*, 351–372.

47. Georgakilas, V., Otyepka, M., Bourlinos, A.B., Chandra, V., Kim, N., Kemp, K.C., Hobza, P., Zboril, R., and Kim, K.S. (2012). Functionalization of graphene: covalent and non-covalent approaches, derivatives and applications. Chem. Rev. *112*, 6156–6214.

48. Samorì, P., Palermo, V., and Feng, X. (2016). Chemical approaches to 2D materials. Adv. Mater. *28*, 6027–6029.

49. Bonaccorso, F., Bartolotta, A., Coleman, J.N., and Backes, C. (2016). 2D-crystal-based functional inks. Adv. Mater. *28*, 6136–6166.

50. Chueh, C.C., Li, C.Z., and Jen, A.K.-Y. (2015). Recent progress and perspective in solution-processed Interfacial materials for efficient and stable polymer and organometal perovskite solar cells. Energy Environ. Sci. *8*, 1160–1189.

51. Taheri, B., Yaghoobi Nia, N.Y., Agresti, A., Pescetelli, S., Ciceroni, C., Del Rio Castillo, A.E., Cinà, L., Bellani, S., Bonaccorso, F., and Di Carlo, A. (2018). Graphene-engineered automated sprayed mesoscopic structure for perovskite device scaling-up. 2D Mater. *5*, 045034.

52. Biccari, F., Gabelloni, F., Burzi, E., Gurioli, M., Pescetelli, S., Agresti, A., Del Rio Castillo, A.E., Ansaldo, A., Kymakis, E., Bonaccorso, F., et al. (2017). Graphene-based electron transport layers in perovskite solar cells: a step-up for an efficient carrier collection. Adv. Energy Mater. *7*, 1701349.

53. Busby, Y., Agresti, A., Pescetelli, S., Di Carlo, A., Noel, C., Pireaux, J.J., and Houssiau, L. (2018). Aging effects in interface-engineered perovskite solar cells with 2D nanomaterials: a depth profile analysis. Mater. Today Energy *9*, 1–10.

54. Volonakis, G., and Giustino, F. (2015). Ferroelectric graphene-perovskite interfaces. J. Phys. Chem. Lett. *6*, 2496–2502.

55. Ramírez Quiroz, C.O., Spyropoulos, G.D., Salvador, M., Roch, L.M., Berlinghof, M., Darío Perea, J., Forberich, K., Dion-Bertrand, L.I., Schrenker, N.J., Classen, A., et al. (2019). Interface molecular engineering for laminated monolithic perovskite/silicon tandem solar cells with 80.4% fill factor. Adv. Funct. Mater. *29*, 1901476.

56. Gösele, U., and Tong, Q.-Y. (1998). Semiconductor wafer bonding. Annu. Rev. Mater. Sci. *28*, 215–241.

57. Moriceau, H., Rieutord, F., Fournel, F., Le Tiec, Y., Di Cioccio, L., Morales, C., Charvet, A.M., and Deguet, C. (2010). Overview of recent direct wafer bonding advances and applications. Adv. Nat. Sci. Nanosci. Nanotechnol. *1*, 043004.

58. Derendorf, K., Essig, S., Oliva, E., Klinger, V., Roesener, T., Philipps, S.P., Benick, J., Hermle, M., Schachtner, M., Siefer, G., et al. (2013). Fabrication of GaInP/GaAs//Si solar cells by surface activated direct wafer bonding. IEEE J. Photovoltaics *3*, 1423–1428.

59. Saliba, M., Matsui, T., Seo, J.Y., Domanski, K., Correa-Baena, J.P., Nazeeruddin, M.K., Zakeeruddin, S.M., Tress, W., Abate, A., Hagfeldt, A., Grätzel, M., et al. (2016). Cesium-containing triple cation perovskite solar cells: improved stability, reproducibility and high efficiency. Energy Environ. Sci. *9*, 1989–1997.

60. Coutts, T.J., Emery, K.A., and Scott Ward, J.S. (2002). Modeled performance of polycrystalline thin-film tandem solar cells. Prog. Photovolt. Res. Appl. *10*, 195–203.

61. DeWolf, S., Descoeudres, A., Holman, Z.C., and Ballif, C. (2012). High-efficiency silicon heterojunction solar cells: a review. Green. *2*, 7–24.

62. Ono, L.K., Juarez-Perez, E.J., and Qi, Y. (2017). Progress on perovskite materials and solar cells with mixed cations and halide anions. ACS Appl. Mater. Interfaces *9*, 30197–30246.

63. Hoke, E.T., Slotcavage, D.J., Dohner, E.R., Bowring, A.R., Karunadasa, H.I., and McGehee, M.D. (2015). Reversible photo-induced trap formation in mixed-halide hybrid perovskites for photovoltaics. Chem. Sci. *6*, 613–617.

64. Saliba, M., Correa-Baena, J.P., Wolff, C.M., Stolterfoht, M., Phung, N., Albrecht, S., Neher, D., and Abate, A. (2018). How to make over 20% efficient perovskite solar cells in regular (n-i-p) and inverted (p-i-n) architectures. Chem. Mater. *30*, 4193–4201.

65. Kanda, H., Uzum, A., Nishino, H., Umeyama, T., Imahori, H., Ishikawa, Y., Uraoka, Y., and Ito, S. (2016). Interface optoelectronics engineering for mechanically stacked tandem solar cells based on perovskite and silicon. ACS Appl. Mater. Interfaces *8*, 33553–33561.

66. Werner, J., Dubuis, G., Walter, A., Löper, P., Moon, S.J., Nicolay, S., Morales-Masis, M., De Wolf, S., Niesen, B., and Ballif, C. (2015). Sputtered rear electrode with broadband transparency for perovskite solar cells. Sol. Energy Mater. Sol. Cells *141*, 407–413.

67. Werner, J., Weng, C.H., Walter, A., Fesquet, L., Seif, J.P., De Wolf, S., Niesen, B., and Ballif, C. (2016). Efficient monolithic perovskite/silicon tandem solar cell with cell area >1 cm^2. J. Phys. Chem. Lett. *7*, 161–166.

68. Zheng, J., Lau, C.F.J., Mehrvarz, H., Ma, F.J., Jiang, Y., Deng, X., Soeriyadi, A., Kim, J., Zhang, M., Hu, L., et al. (2018). Large area efficient interface layer free monolithic perovskite/homo-junction-silicon tandem solar cell with over 20% efficiency. Energy Environ. Sci. *11*, 2432–2443.

69. Bush, K.A., Palmstrom, A.F., Yu, Z.J., Boccard, M., Cheacharoen, R., Mailoa, J.P., McMeekin, D.P., Hoye, R.L.Z., Bailie, C.D., Leijtens, T., et al. (2017). .23.6%-efficient monolithic perovskite/silicon tandem solar cells With improved stability. Nat. Energy *2*, 2.

70. Liu, P., Liu, X., Lyu, L., Xie, H., Zhang, H., Niu, D., Huang, H., Bi, C., Xiao, Z., Huang, J., and Gao, Y. (2015). Interfacial electronic structure at the CH3NH3PbI3/MoOx interface. Appl. Phys. Lett. *106*, 193903.

71. Schulz, P., Tiepelt, J.O., Christians, J.A., Levine, I., Edri, E., Sanehira, E.M., Hodes, G., Cahen, D., and Kahn, A. (2016). High-work-function molybdenum oxide hole extraction contacts in hybrid organic-inorganic perovskite solar cells. ACS Appl. Mater. Interfaces *8*, 31491–31499.

72. Sánchez del Río, M., and Dejus, R.J. (2011). XOP v2.4: recent developments of the x-ray optics software toolkit. In Advances in Computational Methods for X-Ray Optics II, M. Sanchez del Rio and O. Chubar, eds. (SPIE), p. 814115.

73. Filipič, M., Löper, P., Niesen, B., De Wolf, S., Krč, J., Ballif, C., and Topič, M. (2015). CH(3)NH(3)PbI(3) perovskite/silicon tandem solar cells: characterization based optical simulations. Opt. Express *23*, A263–A278.

74. Miandal, K., Tak, H.H., Mohamad, K.A., Chee, F.P., and Alias, A. (2017). The structural and optical properties of poly(triarylamine) (PTAA) thin films prepared at different spin rate using spin coating method. Adv. Sci. Lett. *23*, 1337–1339.

75. Werner, J., Nogay, G., Sahli, F., Yang, T.C.J., Bräuninger, M., Christmann, G., Walter, A., Kamino, B.A., Fiala, P., Löper, P., et al. (2018). Complex refractive indices of cesium-formamidinium-based mixed-halide perovskites with optical band gaps from 1.5 to 1.8 eV. ACS Energy Lett. *3*, 742–747.

76. Bender, M., Seelig, W., Daube, C., Frankenberger, H., Ocker, B., and Stollenwerk, J. (1998). Dependence of film composition and thicknesses on optical and electrical properties of ITO-metal-ITO multilayers. Thin Solid Films *326*, 67–71.

77. Hawash, Z., Ono, L.K., and Qi, Y. (2018). Recent advances in spiro-MeOTAD hole transport material and its applications in organic–inorganic halide perovskite solar cells. Adv. Mater. Interfaces *5*, 1700623.

78. Marinova, N., Tress, W., Humphry-Baker, R., Dar, M.I., Bojinov, V., Zakeeruddin, S.M., Nazeeruddin, M.K., and Grätzel, M. (2015). Light harvesting and charge recombination in CH3NH3PbI3 perovskite solar cells studied by hole transport layer thickness variation. ACS Nano *9*, 4200–4209.

79. You, P., Liu, Z., Tai, Q., Liu, S., and Yan, F. (2015). Efficient semitransparent perovskite solar cells with graphene electrodes. Adv. Mater. *27*, 3632–3638.

80. Bailie, C.D., Christoforo, M.G., Mailoa, J.P., Bowring, A.R., Unger, E.L., Nguyen, W.H., Burschka, J., Pellet, N., Lee, J.Z., Grätzel, M., et al. (2015). Semi-transparent perovskite solar cells for tandems with silicon and CIGS. Energy Environ. Sci. *8*, 956–963.

81. Taguchi, M., Yano, A., Tohoda, S., Matsuyama, K., Nakamura, Y., Nishiwaki, T., Fujita, K., and

Maruyama, E. (2014). .24.7% Record efficiency HIT solar cell on thin silicon wafer. IEEE J. Photovoltaics *4*, 96–99.

82. Elumalai, N.K., and Uddin, A. (2016). Hysteresis in organic-inorganic hybrid perovskite solar cells. Sol. Energy Mater. Sol. Cells *157*, 476–509.

83. Chen, B., Yang, M., Priya, S., and Zhu, K. (2016). Origin of J-V hysteresis in perovskite solar cells. J. Phys. Chem. Lett. *7*, 905–917.

84. Unger, E.L., Hoke, E.T., Bailie, C.D., Nguyen, W.H., Bowring, A.R., Heumüller, T., Christoforo, M.G., and McGehee, M.D. (2014). Hysteresis and transient behavior in current-voltage measurements of hybrid-perovskite absorber solar cells. Energy Environ. Sci. *7*, 3690–3698.

85. Tress, W., Marinova, N., Moehl, T., Zakeeruddin, S.M., Nazeeruddin, M.K., and Grätzel, M. (2015). Understanding the rate-dependent J-V hysteresis, slow time component, and aging in CH 3 NH 3 PbI 3 perovskite solar cells: the role of a compensated electric field. Energy Environ. Sci. *8*, 995–1004.

86. Zhao, Y., Liang, C., Zhang, H., Li, D., Tian, D., Li, G., Jing, X., Zhang, W., Xiao, W., Liu, Q., et al. (2015). Anomalously large interface charge in polarity-switchable photovoltaic devices: an indication of mobile ions in organic-inorganic halide perovskites. Energy Environ. Sci. *8*, 1256–1260.

87. Shao, Y., Xiao, Z., Bi, C., Yuan, Y., and Huang, J. (2014). Origin and elimination of photocurrent hysteresis by fullerene passivation in CH3NH3PbI3 planar heterojunction solar cells. Nat. Commun. *5*, 5784.

88. Matteocci, F., Cinà, L., Lamanna, E., Cacovich, S., Divitini, G., Midgley, P.A., Ducati, C., and Di Carlo, A. (2016). Encapsulation for long-term stability enhancement of perovskite solar cells. Nano Energy *30*, 162–172.

89. Li, Z., Zhao, Y., Wang, X., Sun, Y., Zhao, Z., Li, Y., Zhou, H., and Chen, Q. (2018). Cost analysis of perovskite tandem photovoltaics. Joule *2*, 1559–1572.

90. Song, Z., McElvany, C.L., Phillips, A.B., Celik, I., Krantz, P.W., Watthage, S.C., Liyanage, G.K., Apul, D., and Heben, M.J. (2017). A technoeconomic analysis of perovskite solar module manufacturing with low-cost materials and techniques. Energy Environ. Sci. *10*, 1297–1305.

91. Celik, I., Phillips, A.B., Song, Z., Yan, Y., Ellingson, R.J., Heben, M.J., and Apul, D. (2017). Environmental analysis of perovskites and other relevant solar cell technologies in a tandem configuration. Energy Environ. Sci. *10*, 1874–1884.

92. Adachi, D., Hernández, J.L., and Yamamoto, K. (2015). Impact of carrier recombination on fill factor for large area heterojunction crystalline silicon solar cell with 25.1% efficiency. Appl. Phys. Lett. *107*, 233506.